Molecular beam epitaxy of antiferromagnetic (MnBi$_2$Te$_4$)(Bi$_2$Te$_3$) thin films on BaF$_2$ (111)

P. Kagerer [ID], C. I. Fornari [ID], S. Buchberger, S. L. Morelhão [ID], R. C. Vidal, A. Tcakaev [ID], V. Zabolotnyy, E. Weschke, V. Hinkov [ID], M. Kamp [ID], B. Büchner, A. Isaeva [ID], H. Bentmann, and F. Reinert

View Online   Export Citation   CrossMark

ARTICLES YOU MAY BE INTERESTED IN

AIP Publishing

Molecular beam epitaxy of antiferromagnetic $(MnBi_2Te_4)(Bi_2Te_3)$ thin films on BaF_2 (111)

View Online Export Citation CrossMark

P. Kagerer,[1,2] C. I. Fornari,[1,2,a)] S. Buchberger,[1,2] S. L. Morelhão,[3] R. C. Vidal,[1,2] A. Tcakaev,[4] V. Zabolotnyy,[4] E. Weschke,[5] V. Hinkov,[4] M. Kamp,[6] B. Büchner,[2,7,8] A. Isaeva,[2,7,8] H. Bentmann,[1,2,b)] and F. Reinert[1,2]

AFFILIATIONS

[1]Experimentelle Physik VII, Universität Würzburg, Am Hubland, D-97074 Würzburg, Germany
[2]Würzburg-Dresden Cluster of Excellence ct.qmat, D-97074 Würzburg, Germany and Würzburg-Dresden Cluster of Excellence ct.qmat, D-01062 Dresden, Germany
[3]Instituto de Física, Universidade de São Paulo, 05508-090 São Paulo, SP, Brazil
[4]Experimentelle Physik IV, Universität Würzburg, Am Hubland, D-97074 Würzburg, Germany
[5]Helmholtz-Zentrum Berlin für Materialien und Energie, Albert-Einstein-Str. 15, D-12489 Berlin, Germany
[6]Physikalisches Institut and Röntgen-Center for Complex Material Systems (RCCM), Fakultät für Physik und Astronomie, Universität Würzburg, Am Hubland, D-97074 Würzburg, Germany
[7]Leibniz IFW Dresden, Helmholtzstr. 20, 01069 Dresden, Germany
[8]Institut für Festkörper- und Materialphysik, Technische Universität Dresden, D-01062 Dresden, Germany

[a)]Author to whom correspondence should be addressed: celso.fornari@physik.uni-wuerzburg.de
[b)]Electronic mail: Hendrik.Bentmann@physik.uni-wuerzburg.de

ABSTRACT

The layered van der Waals compounds $(MnBi_2Te_4)(Bi_2Te_3)$ were recently established as the first intrinsic magnetic topological insulators. We report a study on the epitaxial growth of $(MnBi_2Te_4)_m(Bi_2Te_3)_n$ films based on the co-deposition of MnTe and Bi_2Te_3 on BaF_2 (111) substrates. X-ray diffraction and scanning transmission electron microscopy evidence the formation of multilayers of stacked $MnBi_2Te_4$ septuple layers and Bi_2Te_3 quintuple layers with a predominance of $MnBi_2Te_4$. The elemental composition and morphology of the films is further characterized by x-ray photoemission spectroscopy and atomic force microscopy. X-ray magnetic circular and linear dichroism spectra are comparable to those obtained for $MnBi_2Te_4$ single crystals and confirm antiferromagnetic order in the films.

I. INTRODUCTION

The combination of non-trivial electronic band topology and magnetism is presently attracting broad interest in condensed matter physics. A prominent example is the quantum anomalous Hall (QAH) effect that has been realized in magnetically doped topological insulators such as Cr- and V-doped $(Bi, Sb)_2Te_3$.[1,2] Although rather high critical temperatures can be achieved in these systems,[2] the observation of the QAH effect has typically been limited to the mK temperature regime.[1,2] More recently, so-called intrinsic magnetic topological insulators (IMTIs) have been introduced.[3,4] These materials intrinsically combine long-range magnetic order with an inverted band structure and, thus, do not require magnetic doping. An important class of IMTI is the magnetic van der Waals system $(MnBi_2Te_4)_m(Bi_2Te_3)_n$

(MBT), where $MnBi_2Te_4$ septuple layers (SLs) and non-magnetic Bi_2Te_3 quintuple layers (QLs) are stacked in a layer-wise fashion. In particular, the parent compound $MnBi_2Te_4$ has been established as the first antiferromagnetic three-dimensional TI.[3–9] Moreover, the higher-n compounds $MnBi_4Te_7$[10–13] and $MnBi_6Te_{10}$[10,13–15] have been shown to be IMTIs, with deviating magnetic properties arising from the modified interlayer couplings between the magnetically active Mn lattice planes.

Besides the above-mentioned topological properties in three-dimensional $(MnBi_2Te_4)_m(Bi_2Te_3)_n$, an even richer interplay between topology and magnetism is expected in the two-dimensional (2D) regime.[16–18] Indeed, recent magneto-transport experiments on two-dimensional few-layer flakes of $MnBi_2Te_4$

revealed signatures of the QAH effect[19] and an axion insulator state.[20] Also, in the 2D regime, magnetic proximity effects may be exploited at interfaces of $MnBi_2Te_4$ with other magnetic van der Waals compounds such as CrI_3.[21] In this scenario, it is important to establish the fabrication of $MnBi_2Te_4$-based thin films by molecular beam epitaxy (MBE) in order to provide a basic platform for new physics and devices in the field of IMTI.

Previously, multilayer films of $(MnBi_2Te_4)(Bi_2Te_3)$ and $(MnBi_2Se_4)(Bi_2Se_3)$ with random stacking order were fabricated by co-deposition of the respective elements.[22,23] Such films were QL-rich, where the ratio $\gamma_{SL} = \frac{m}{m+n}$ between the number m of SLs and the total number $m + n$ of SLs and QLs was below $\frac{1}{2}$. In this regime of γ_{SL}, ferromagnetic properties have been reported for $(MnBi_2Te_4)(Bi_2Te_3)$ multilayers with characteristic temperatures of 7–15 K.[23] In other works, $MnBi_2Te_4$ and $MnBi_2Se_4$ films have also been fabricated by complex alternating-layer multi-step growth procedures.[4,24] More recently, the growth of $MnBi_2Te_4$ films by co-deposition of Mn, Bi, and Te on $SrTiO_3$ (111) substrates has been reported.[25] In this work, we report the MBE growth of $(MnBi_2Te_4)_m(Bi_2Te_3)_n$ multilayers by means of co-evaporation of the binary compounds MnTe and Bi_2Te_3 on BaF_2 (111) substrates. The layers are SL-rich with $\gamma_{SL} > 0.7$, as confirmed by scanning transmission electron microscopy (STEM) and x-ray diffraction (XRD) measurements and simulations in model structures. X-ray magnetic circular dichroism (XMCD) and x-ray magnetic linear dichroism (XMLD) experiments confirm antiferromagnetic order in the layers. Our results establish a flexible approach for the epitaxial growth of high-quality IMTI thin films for advanced experimental investigations and device applications.

II. EXPERIMENTAL DETAILS

The growth of Bi_2Te_3 thin films on BaF_2 (111) substrates is well established, and depending on the growth conditions, highly ordered epilayers without tellurium deficiency are obtained.[26,27] Even though lattice mismatch is not the most critical parameter for epitaxy of van der Waals compounds, refined XRD investigations demonstrated that a slight increase of the van der Waals forces can prevent the relaxation of the layers.[28] BaF_2 on the (111) plane is almost lattice matched to the in-plane Bi_2Te_3 lattice constant ($\Delta_a = 0.04\%$)[29] and in very good agreement to the in-plane lattice constant of $MnBi_2Te_4$ ($\Delta_a = 1.2\%$). Moreover, BaF_2 is transparent from the UV to the far IR regime and highly insulating, with an energy gap around 9 eV. These characteristics make barium fluoride an excellent candidate to host MBT thin films for both technological applications and scientific investigations.

For this work, $(MnBi_2Te_4)_m(Bi_2Te_3)_n$ thin films were grown on freshly cleaved BaF_2 (111) substrates using effusion cells charged nominally with Bi_2Te_3 and MnTe. The latter were prepared phase-pure by inorganic solid-state reactions.[8] The beam equivalent pressure (BEP) is monitored by an ion gauge before and after each growth. The manganese supply is defined by the ratio of the BEPs as $\Phi_R = BEP_{MnTe}/BEP_{Bi_2Te_3}$. In the case of $\Phi_R = 0$, a pure phase of Bi_2Te_3 ($\gamma_{SL} = 0$) is obtained. The base pressure of the growth chamber is 7×10^{-11} mbar, and the background pressure stays below 5×10^{-8} mbar during deposition. BaF_2 substrates are pre-heated at 350 °C for 10 min before starting deposition. The

substrate temperature was fixed at $T_{SUB} = 280\,°C$ and $BEP_{Bi_2Te_3}$ was kept fixed, resulting in a deposition rate of 0.02 Å/s for the Bi_2Te_3 cell. The Mn supply, through the MnTe effusion cell, was increased up to $\Phi_R = 0.07$. Thus, the samples prepared in this work are labeled by Φ_R, where $\Phi_R = 0$ indicates a pure Bi_2Te_3 ($\gamma_{SL} = 0$) epitaxial film and $\Phi_R = 0.07$ represents our Mn-richest MBT film.

Low energy electron diffraction (LEED) and x-ray photoelectron spectroscopy (XPS) measurements were carried out *in situ* directly after growth, without exposing the sample to air. The XPS measurements were performed with an Al-anode x-ray gun (Al K_α, $h\nu = 1486.6$ eV) and a Scienta SES200 photoelectron analyzer. The LEED experiments were conducted using a ThermoVG Scientific standard LEED apparatus.

XRD measurements were performed with a Bruker high resolution x-ray diffractometer equipped with a Göbel mirror and a Ge (220) monochromator. Cu K_α radiation ($\lambda = 1.5418\,Å$) was used. Long-range $\omega - 2\theta$ scans, along the surface normal direction in the reciprocal space, were performed in the same specular reflection geometry used for measuring grazing incidence x-ray reflectivity curves. The GenX software package[30] was used to calculate the reflectivity curves in order to extract quantitative information.

X-ray diffraction curves were calculated using a set of recursive equations,[31] suitable for layered materials with large d-spacing. It has been successfully applied for the case of Bi_xTe_y homologous series,[32] where Bi double-layers and Bi_2Te_3 QLs coexist even in random stacking order. Here, model structures of $(MnBi_2Te_4)_m(Bi_2Te_3)_n$ films containing a total number $m + n = 20$ of SL and QL building blocks and different compositions
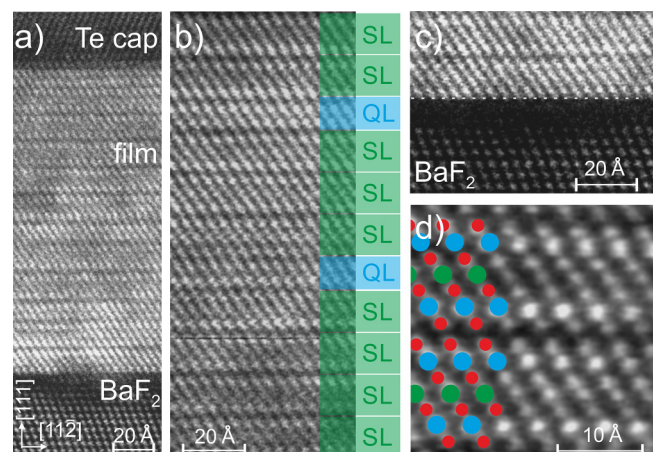
FIG. 1. Scanning transmission electron microscopy (STEM) cross-sectional images of a 15 nm thick MBT film ($\Phi_R = 0.03$) capped with Te. (a) Cross-sectional overview image showing the BaF_2 substrate, the epitaxial layers, and the Te protective capping layer. (b) Detailed view of the structure of the film where septuple layers (SLs) and quintuple layers (QLs) are observed. (c) A detailed view of the interface between the substrate-layer where the first two SLs are clearly observed. (d) Close-up view showing SLs in detail with a representation of the structure as: red—Te, blue—Bi, and green—Mn.

γ_{SL} were considered for XRD simulation. For films with $\gamma_{SL} < 1$ ($n > 0$), the simulated intensity curves stand for average curves over hundreds of model structures with random stacking of n QLs. Bulk lattice parameters were used for all simulations, as well as for the van der Waals gaps. An average gap value was assumed between adjacent SL and QL blocks.

Cross-sectional lamellas for transmission electron microscopy (TEM) studies were prepared at the Wilhelm Conrad Röntgen Research Center for Complex Material System (RCCM) using a FEI Helios Nanolab Dual Beam system using Ga+ ion beam milling. The lateral thickness of the lamellas is estimated to be between 25 and 50 nm. STEM imaging was performed using an uncorrected FEI Titan 80–300 TEM at the RCCM and a probe corrected FEI Titan 80–300 at the IFW.

Atomic force microscopy (AFM) images were acquired with a Bruker dimension icon system in ambient air using a tapping mode. The equipment is installed on an optical table to avoid vibrations. The software package Gwyddion was used for analysis and image processing.[33]

X-ray magnetic circular dichroism (XMCD) and x-ray magnetic linear dichroism (XMLD) measurements were carried out at a high-field diffractometer end station of the UE46 PGM-1

beamline at BESSY II[34] using circularly and linearly polarized photons near the Mn $L_{2,3}$ absorption edges. The data were obtained in the total electron yield (TEY) mode. The protective Te-cap was mechanically removed before the measurements, exposing a pristine surface.[35]

III. RESULTS AND DISCUSSION

Figure 1(a) presents a cross-sectional overview image showing the BaF$_2$ substrate, the MBT epitaxial layer, and the Te protective capping. Figure 1(b) shows a detailed view on the epitaxial MBT layers, where one can observe the van der Waals gaps between the building blocks and distinguish the formation of SLs and QLs. A guide to the eyes is drawn on the right side of the image, indicating SLs (green rectangles) and QLs (blue rectangles). Figure 1(c) presents a detailed image of the interface between film and substrate, showing the formation of the first two SLs. The dashed white line is a guide to the eye. Figure 1(d) displays two SLs on the atomic scale, together with a representation of the structure.

The STEM cross-sectional images obtained from our sample indicate that MBT with a SL-rich composition close to MnBi$_2$Te$_4$ was obtained. The occurrence of QLs randomly distributed in between the SLs was observed. In some cases, two
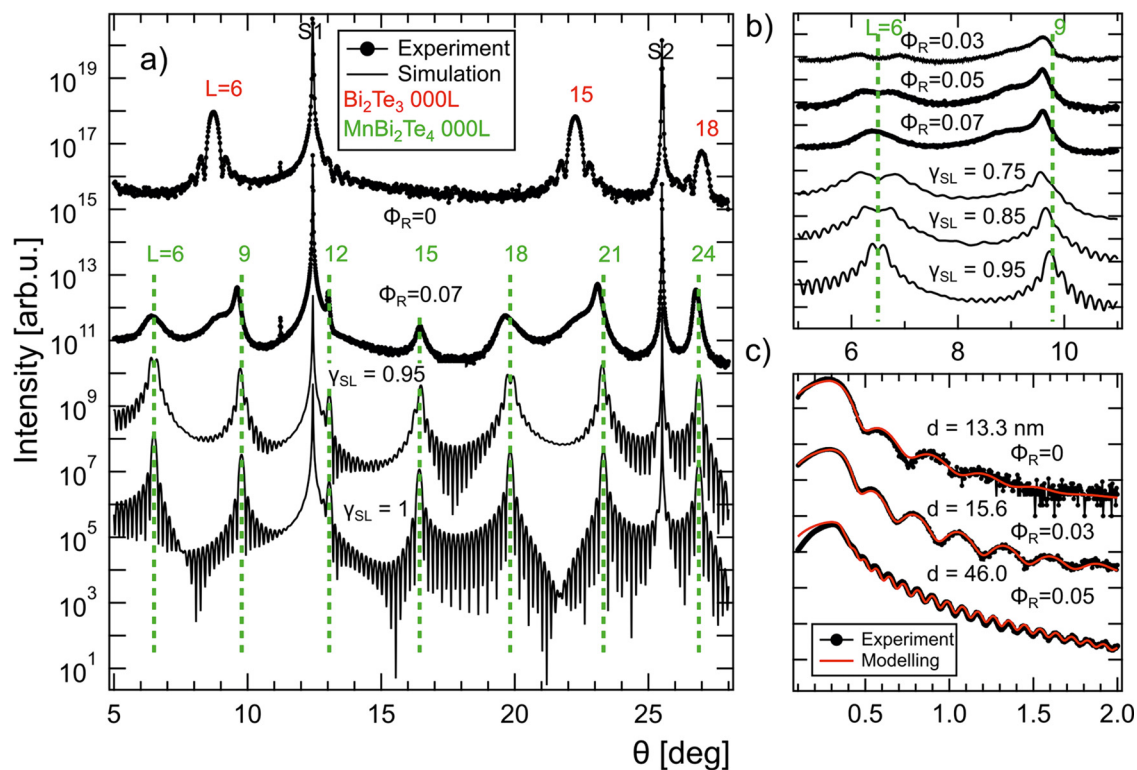
FIG. 2. (a) XRD $\omega - 2\theta$ scans of a Bi$_2$Te$_3$ film (upper curve) and an MBT film (lower curve, $\Phi_R = 0.07$). XRD simulations are shown for stoichiometric MnBi$_2$Te$_4$ (lowest line) and a phase with Bi$_2$Te$_3$ QL intermixture (see text for details). (b) Zoom into the low-θ region showing the evolution of the $L = 6$ peak-splitting with the BEP ratio Φ_R. The measurements are compared to simulations for different SL ratios γ_{SL}. (c) XRR curves for a Bi$_2$Te$_3$ film and two MBT films with $\Phi_R = 0.03$ and $\Phi_R = 0.05$.

adjacent QLs can exist. The sharp interfaces between substrate-film and film-capping layer indicate a high quality of our epilayers and a homogeneous thickness of the layers. Our STEM results indicate the occurrence of approximately 1 QL for every 4 SLs ($\gamma_{SL} = 0.8$).

XRD on long-range $\omega - 2\theta$ scans for evaluation of the film structures are presented in Fig. 2(a). It shows the XRD curves acquired for the Bi_2Te_3 ($\Phi_R = 0$) and MBT ($\Phi_R = 0.07$) films. Besides BaF_2 substrate peaks, reflections 111 (S1) and 222 (S2), only diffraction peaks of 000L film reflections are observed, with L being a multiple of 3. This is an evidence that epitaxy is occurring as expected with the (0001) $Bi_2Te_3/MnBi_2Te_4$ planes parallel to the (111) planes of the BaF_2 substrate.

The Bi_2Te_3 diffraction curve exhibits well-defined interference fringes around the diffraction peaks, indicating a highly ordered stacking of QLs. The stoichiometry of the film is $Bi_2Te_{2.98}$, calculated through the position of the peak $L = 15$,[26] which can be interpreted as 1 Bi bilayer occurring in less than 10% of the film area.[28] These results reinforce the high quality of our Bi_2Te_3 epitaxial films that are used as a starting point to grow $MnBi_2Te_4$. The MBT diffraction curve presents well-defined diffraction peaks located around the theoretical positions of the $MnBi_2Te_4$ phase, as indicated by dashed lines in Figs. 2(a) and 2(b). However, the MBT curve obtained for the highest Mn supply ($\Phi_R = 0.07$) does not present clear interference fringes, which might be an indication of non-uniform film thickness from the perspective of the incidence angles higher than a few degrees. For a slightly lower Mn supply ($\Phi_R = 0.05$), the diffraction peaks $L = 6$, 18, and 30 present a splitting (long-range $\omega - 2\theta$ scan not shown here).

Figure 2(a) shows a simulated curve containing 19 SLs and 1 QL ($\gamma_{SL} = 0.95$) and a curve containing 20 SLs ($\gamma_{SL} = 1$), representing the pure $MnBi_2Te_4$ phase. For the QL-rich phase, a clear splitting in the L6 diffraction peak is observed. This splitting is linearly proportional to the amount of QLs inside the film, allowing us to estimate the stoichiometry of the films as

$$\gamma_{SL} = 1 - 0.258 \cdot \Delta\theta, \quad (1)$$

where θ is given in degrees. Using this equation, we obtain that our epitaxial film grown with $\Phi_R = 0.03$ is composed 70% by SLs ($\gamma_{SL} = 0.7$). This is the sample analyzed by STEM (Fig. 1), where a mean value of $\gamma_{SL} = 0.8$ was addressed. These results are in very good agreement and reinforce the capability of our XRD model in estimating the MBT phases. The MBT film grown with $\Phi_R = 0.05$ is composed 87% by SLs ($\gamma_{SL} = 0.87$), while the one prepared with $\Phi_R = 0.07$ presents no observable splitting, indicating that the epilayers are composed predominantly by SLs ($\gamma_{SL} > 0.95$).

X-ray reflectivity curves were measured for the Bi_2Te_3 ($\Phi_R = 0$) and two MBT films with $\Phi_R = 0.03$ and 0.05, respectively. Figure 2(c) presents the experimental data (circles) together with the best fitting curves (solid lines). All films exhibit very well-defined interference fringes, indicating a homogeneous film thickness with smooth interface and surface along the whole substrate area. The calculated thickness of the Bi_2Te_3 sample is 133 Å with a surface roughness of 4.7 Å. The MBT films were grown for different time, resulting in a thickness of 156 and 460 Å. The surface
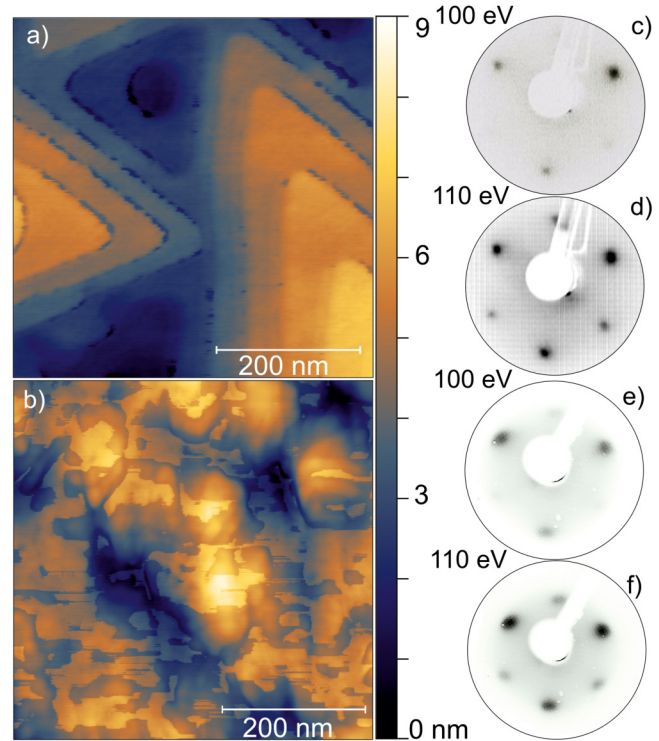

FIG. 3. AFM topography images of (a) a Bi_2Te_3 and (b) a MBT film ($\Phi_R = 0.05$) grown on BaF_2(111). (c)–(f) LEED images for as-grown (c)–(d) Bi_2Te_3 and (e)–(f) MBT ($\Phi_R = 0.07$). LEED data were taken at primary energies of $E_0 = 100$ eV in (c) and (e) and $E_0 = 110$ eV in (d) and (f). The threefold symmetric patterns in (c) and (e) indicate negligible twin-domain formation.
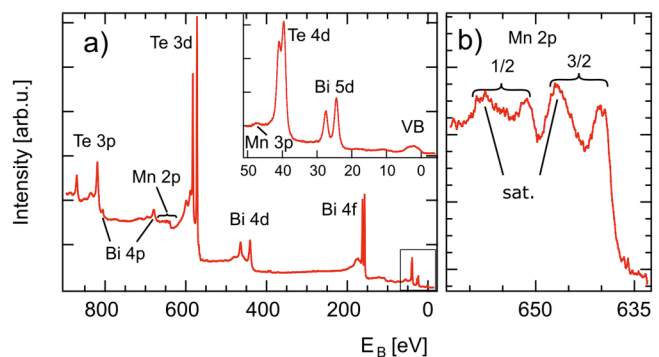

FIG. 4. (a) XPS overview dataset for a MBT film ($\Phi_R = 0.07$), showing core-level lines of the elements Mn, Bi, and Te, and no indications of contamination. The inset shows a detail spectrum of the shallow core levels. (b) XPS dataset of the Mn 2p core level. Satellites at approximately 6 eV below the respective main lines are indicated.

roughness for both MBT films is lower than 4.9 Å. The density of the films was kept as an open parameter during the fit procedure, resulting in $7.7\,g/cm^3$ for the Bi_2Te_3 sample and $7.3\,g/cm^3$ for the MBT samples. These values are in excellent agreement with the tabulated values. The precise control of the thicknesses, low surface roughness values, and sharp interfaces of our samples indicate that it is possible to reduce the thickness of the films down to a few SLs in order to reach the 2D regime.[16]

In order to investigate the surface morphology of the thin films, atomic force microscopy (AFM) was employed and the results are shown in Figs. 3(a) and 3(b). The typical spiral-like triangular domains from the Bi_2Te_3 phase [Fig. 3(a)] can be clearly observed, while an undefined morphology is observed for the MBT film grown with $\Phi_R = 0.05$ [Fig. 3(b)], although surface morphology is weakly related to the film structure.[36] For both measurements, layered steps can be clearly distinguished on the surface. A surface roughness of 13 Å is obtained for the Bi_2Te_3

film and 14.7 Å for the MBT film, prepared with $\Phi_R = 0.05$. Low electron energy diffraction (LEED) was employed to check the surface. Figure 3 shows the LEED images of a 15 nm thick Bi_2Te_3 (c)–(d) and a MBT $\Phi_R = 0.07$ (e)–(f) films. Both samples show bright spots forming the hexagonal pattern characteristic of the three-fold symmetry, indicating a highly ordered surface with low amount of twinning. A slight increase of the diffraction spots and background intensity is observed for the MBT film, indicating an increase of structural disorder when compared to the pure Bi_2Te_3 phase.

XPS data obtained at $h\nu = 1486.6\,eV$ (Al K_α) is presented in Fig. 4(a). The core-level lines of Te, Bi, and Mn are observed. Figure 4(b) shows a detailed scan of the Mn 2p line, which exhibits a rather complex multiplet fine structure. In particular, the $2p_{3/2}$ and $2p_{1/2}$ levels both display a satellite feature approximately 6 eV below the respective main lines. This satellite has been observed in other Mn compounds and can be tentatively associated with a Mn^{2+}
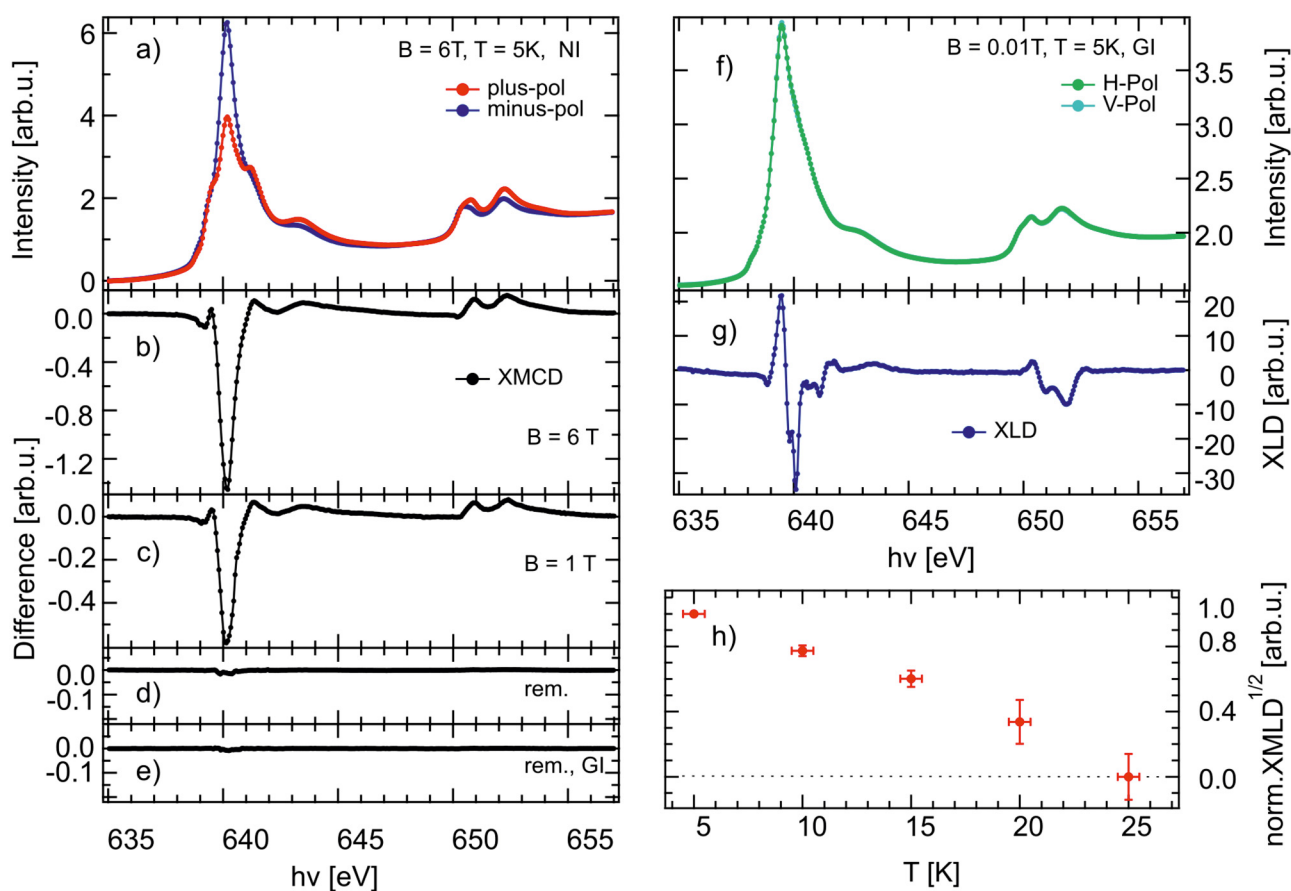

FIG. 5. XMCD and XMLD datasets for a MBT film ($\Phi_R = 0.03$) obtained at the Mn $L_{2,3}$ absorption edge at $T = 5\,K$. (a) X-ray absorption spectra (XAS) for positive and negative circular polarizations measured in normal incidence and $B = 6\,T$. (b) Corresponding XMCD signal. (c) and (d) XMCD signal measured at $B = 1\,T$ and in remanence, respectively. (e) XMCD signal measured for remanence and for grazing light incidence (GI), with an angle of incidence of $60°$. (f) XAS spectra measured for linear horizontal (H) and vertical (V) polarization in grazing incidence and in the absence of an external field at $T = 5\,K$. (g) Resulting XMLD signal. (h) Temperature dependence of the square root of the XMLD signal, normalized to the value at $T = 5\,K$.

oxidation state,[37] as expected for $MnBi_2Te_4$. The overall line shape of the Mn 2p level, including the pronounced satellites, is comparable to the one observed for $MnBi_2Te_4$ single crystals,[5,8] further supporting the results of our structural analysis by STEM and XRD.

To investigate the magnetic properties of the MBT films, we performed XMCD and XMLD measurements at the Mn $L_{2,3}$ absorption edge (Fig. 5). At external fields of 6 T and 1 T, a sizable XMCD signal is observed in normal light incidence ($T = 5$ K), evidencing a magnetic polarization of the Mn ions [Figs. 5(a)–5(c)]. After removing the external field, the XMCD collapses, both for normal and grazing light incidence, as shown in Figs. 5(d) and 5(e). This behavior is consistent with an antiferromagnetic ordering and closely matches previous XMCD results for $MnBi_2Te_4$ single crystals.[3,5] XLD measurements performed in grazing light incidence and without the external field show a significant signal at $T = 5$ K [Figs. 5(f) and 5(g)]. The XLD signal gradually diminishes with increasing temperature, confirming its magnetic origin as opposed to a crystal-field effect. These observations are again similar to previous XLD results for $MnBi_2Te_4$ single crystals and further confirm an antiferromagnetic state.[5,8] From the temperature dependence of the XLD signal in Fig. 5(h), we estimate a Néel temperature between 20 and 25 K, which is comparable to $MnBi_2Te_4$ bulk single crystals[3,8] and significantly larger than for $MnBi_4Te_7$.[10,11] The observed x-ray absorption spectra (XAS), XMCD, and XLD line shapes closely match those observed for bulk $MnBi_2Te_4$,[3,5,8] in line with the formation of $MnBi_2Te_4$ SL in the films revealed by our XRD and STEM results.
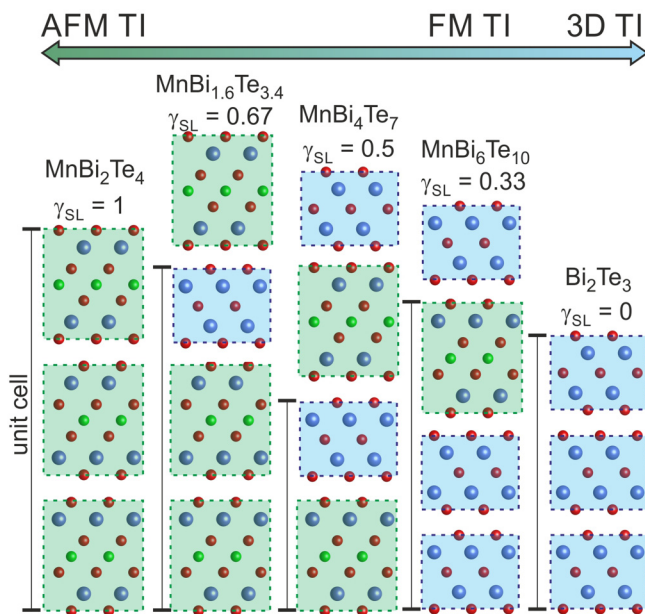
Overall, our results indicate that, by controlling the Mn supply during the growth (Φ_R), it is possible to change the composition of the films continuously from the non-magnetic 3D TI Bi_2Te_3 to the intrinsic antiferromagnetic TI $MnBi_2Te_4$, as sketched in Fig. 6, with additional intermediate phases, such as TI with ferromagnetic ordering.[23] This provides a rich playground to explore the interplay of magnetism and topology in this tunable material system. Moreover, due to the high control and reproducibility of the epitaxial growth, decreasing the layer thickness to explore the 3D to 2D transition regimes and heterostructures with other materials will become within reach.

IV. SUMMARY

We carried out molecular beam epitaxy of $(MnBi_2Te_4)_m(Bi_2Te_3)_n$ multilayers based on co-deposition of MnTe and Bi_2Te_3 on BaF_2 (111) substrates. STEM and XRD experiments show a predominance of $MnBi_2Te_4$ septuple layers, with ratios γ_{SL} between 0.7 and close to 1. By using XMCD and XMLD, we confirm antiferromagnetic order in the layers, in accordance with previous findings on bulk single crystals. Our results establish a flexible approach for the fabrication of thin films of intrinsic magnetic topological insulators, which will be of interest for realizing exotic 2D topological phenomena and for applications in the research fields of antiferromagnetic spintronics and magnetic van der Waals materials.

DATA AVAILABILITY

The data that support the findings of this study are available from the corresponding author upon reasonable request.

FIG. 6. Crystal structure representation of the $(MnBi_2Te_4)_m(Bi_2Te_3)_n$ series, ranging from the antiferromagnetic (AFM) TI $MnBi_2Te_4$ ($\gamma_{SL} = 1$), over ferromagnetic (FM) TI states (low γ_{SL}) to the three-dimensional (3D) non-magnetic topological insulator Bi_2Te_3 ($\gamma_{SL} = 0$).

REFERENCES

[1]C.-Z. Chang, J. Zhang, X. Feng, J. Shen, Z. Zhang, M. Guo, K. Li, Y. Ou, P. Wei, L.-L. Wang et al., Science **340**, 167 (2013).

[2]C.-Z. Chang, W. Zhao, D. Y. Kim, H. Zhang, B. A. Assaf, D. Heiman, S.-C. Zhang, C. Liu, M. H. W. Chan, and J. S. Moodera, Nat. Mater. **14**, 473 (2015).

[3]M. M. Otrokov, I. I. Klimovskikh, H. Bentmann, D. Estyunin, A. Zeugner, Z. S. Aliev, S. Gaß, A. U. B. Wolter, A. V. Koroleva, A. M. Shikin et al., Nature **576**, 416 (2019).

[4]Y. Gong, J. Guo, J. Li, K. Zhu, M. Liao, X. Liu, Q. Zhang, L. Gu, L. Tang, X. Feng et al., Chin. Phys. Lett. **36**, 076801 (2019).

[5]R. C. Vidal, H. Bentmann, T. R. F. Peixoto, A. Zeugner, S. Moser, C.-H. Min, S. Schatz, K. Kißner, M. Ünzelmann, C. I. Fornari et al., Phys. Rev. B **100**, 121104 (2019).

[6]Y.-J. Hao, P. Liu, Y. Feng, X.-M. Ma, E. F. Schwier, M. Arita, S. Kumar, C. Hu, R. Lu, M. Zeng et al., Phys. Rev. X **9**, 041038 (2019).

[7]Y. J. Chen, L. X. Xu, J. H. Li, Y. W. Li, H. Y. Wang, C. F. Zhang, H. Li, Y. Wu, A. J. Liang, C. Chen et al., Phys. Rev. X **9**, 041040 (2019).

[8]A. Zeugner, F. Nietschke, A. U. B. Wolter, S. Gaß, R. C. Vidal, T. R. F. Peixoto, D. Pohl, C. Damm, A. Lubk, R. Hentrich et al., Chem. Mater. **31**, 2795 (2019).

[9]J.-Q. Yan, Q. Zhang, T. Heitmann, Z. Huang, K. Y. Chen, J.-G. Cheng, W. Wu, D. Vaknin, B. C. Sales, and R. J. McQueeney, Phys. Rev. Mater. **3**, 064202 (2019).

[10]J. Wu, F. Liu, M. Sasase, K. Ienaga, Y. Obata, R. Yukawa, K. Horiba, H. Kumigashira, S. Okuma, T. Inoshita et al., Sci. Adv. **5**, eaax9989 (2019).

[11]R. C. Vidal, A. Zeugner, J. I. Facio, R. Ray, M. H. Haghighi, A. U. B. Wolter, L. T. Corredor Bohorquez, F. Caglieris, S. Moser, T. Figgemeier et al., Phys. Rev. X **9**, 041065 (2019).

[12]C. Hu, K. N. Gordon, P. Liu, J. Liu, X. Zhou, P. Hao, D. Narayan, E. Emmanouilidou, H. Sun, Y. Liu et al., Nat. Commun. **11**, 97 (2020).

[13]J.-Q. Yan, Y. H. Liu, D. S. Parker, Y. Wu, A. A. Aczel, M. Matsuda, M. A. McGuire, and B. C. Sales, Phys. Rev. Mater. **4**, 054202 (2020).

[14]S. Tian, S. Gao, S. Nie, Y. Qian, C. Gong, Y. Fu, H. Li, W. Fan, P. Zhang, T. Kondo et al., Phys. Rev. B **102**, 035144 (2020).

[15]N. H. Jo, L.-L. Wang, R.-J. Slager, J. Yan, Y. Wu, K. Lee, B. Schrunk, A. Vishwanath, and A. Kaminski, Phys. Rev. B **102**, 045130 (2020).

[16]M. M. Otrokov, I. P. Rusinov, M. Blanco-Rey, M. Hoffmann, A. Y. Vyazovskaya, S. V. Eremeev, A. Ernst, P. M. Echenique, A. Arnau, and E. V. Chulkov, Phys. Rev. Lett. **122**, 107202 (2019).

[17]D. Zhang, M. Shi, T. Zhu, D. Xing, H. Zhang, and J. Wang, Phys. Rev. Lett. **122**, 206401 (2019).

[18]J. Li, Y. Li, S. Du, Z. Wang, B.-L. Gu, S.-C. Zhang, K. He, W. Duan, and Y. Xu, Sci. Adv. **5**, eaaw5685 (2019).

[19]Y. Deng, Y. Yu, M. Z. Shi, Z. Guo, Z. Xu, J. Wang, X. H. Chen, and Y. Zhang, Science **367**, 895 (2020).

[20]C. Liu, Y. Wang, H. Li, Y. Wu, Y. Li, J. Li, K. He, Y. Xu, J. Zhang, and Y. Wang, Nat. Mater. **19**, 522 (2020).

[21]H. Fu, C.-X. Liu, and B. Yan, Sci. Adv. **6**, eaaz0948 (2020).

[22]J. A. Hagmann, X. Li, S. Chowdhury, S.-N. Dong, S. Rouvimov, S. J. Pookpanratana, K. M. Yu, T. A. Orlova, T. B. Bolin, C. U. Segre et al., New J. Phys. **19**, 085002 (2017).

[23]E. D. L. Rienks, S. Wimmer, J. Sánchez-Barriga, O. Caha, P. S. Mandal, J. Růžička, A. Ney, H. Steiner, V. V. Volobuev, H. Groiss et al., Nature **576**, 423 (2019).

[24]T. Zhu, A. J. Bishop, T. Zhou, M. Zhu, D. J. O'Hara, A. A. Baker, S. Cheng, R. C. Walko, J. J. Repicky, J. A. Gupta et al., arXiv:2003.07938 (2020), p. 085002.

[25]K. Zhu, Y. Bai, X. Hong, Z. Geng, Y. Jiang, R. Liu, Y. Li, M. Shi, L. Wang, W. Li et al., J. Phys.: Condens. Matter **32**, 475002 (2020).

[26]C. I. Fornari, P. H. O. Rappl, S. L. Morelhão, and E. Abramof, J. Appl. Phys. **119**, 165303 (2016).

[27]C. I. Fornari, P. H. O. Rappl, S. L. Morelhão, G. Fornari, J. S. Travelho, S. de Castro, M. J. P. Pirralho, F. S. Pena, M. L. Peres, and E. Abramof, Mater. Res. Express **5**, 116410 (2018).

[28]S. Morelhão, S. Kycia, S. Netzke, C. I. Fornari, P. H. O. Rappl, and E. Abramof, Appl. Phys. Lett. **112**, 101903 (2018).

[29]O. Caha, A. Dubroka, J. Humlíček, V. Holý, H. Steiner, M. Ul-Hassan, J. Sánchez-Barriga, O. Rader, T. N. Stanislavchuk, A. A. Sirenko et al., Cryst. Growth Des. **13**, 3365 (2013).

[30]M. Björck and G. Andersson, J. Appl. Crystallogr. **40**, 1174 (2007).

[31]S. L. Morelhão, *Computer Simulation Tools for X-ray Analysis*, Graduate Texts in Physics (Springer International Publishing, Cham, 2016), ISBN 978-3-319-19553-7.

[32]S. L. Morelhão, C. I. Fornari, P. H. O. Rappl, and E. Abramof, J. Appl. Crystallogr. **50**, 399 (2017).

[33]D. Nečas and P. Klapetek, Open Phys. **10**, 181 (2012).

[34]E. Weschke and E. Schierle, J. Large-Scale Res. Facil. **4**, 127 (2018).

[35]C. I. Fornari, P. H. O. Rappl, S. L. Morelhão, T. R. F. Peixoto, H. Bentmann, F. Reinert, and E. Abramof, APL Mater. **4**, 106107 (2016).

[36]C. I. Fornari, E. Abramof, P. H. O. Rappl, S. W. Kycia, and S. L. Morelhão, MRS Adv. **5**, 1891 (2020).

[37]M. C. Biesinger, B. P. Payne, A. P. Grosvenor, L. W. M. Lau, A. R. Gerson, and R. S. C. Smart, Appl. Surf. Sci. **257**, 2717 (2011).